Polar Stratospheric Cloud Observations from the OMPS Limb Profiler

Matthew T. DeLand[1] and Mark R. Schoeberl[2]

[1]Science Systems and Applications, Inc. (SSAI), Lanham, MD, USA
[2]Science and Technology Corporation, Columbia, MD, USA

Corresponding author: Matthew DeLand (matthew.deland@ssaihq.com)

Key Points:

- Polar stratospheric clouds (PSCs) strongly influence the magnitude of springtime polar ozone depletion
- Ozone Mapping and Profiler Suite (OMPS) Limb Profiler (LP) measurements, available since 2012, can identify PSCs and characterize their distribution
- Northern Hemisphere PSC occurrence frequency and area have more interannual variability than Southern Hemisphere PSC results

Abstract

The frequency and spatial distribution of polar stratospheric clouds (PSCs) has a strong influence on the magnitude of springtime ozone depletion in polar regions. We use Ozone Mapping and Profiler Suite (OMPS) Limb Profiler (LP) satellite measurements to identify PSCs and characterize their distribution. Concurrent water vapor and nitric acid profiles from Aura Microwave Limb Sounder (MLS) measurements are used to determine the approximate temperature threshold for PSC formation. OMPS LP daytime measurements have limited coverage of the polar vortex region during winter months, with increasing coverage as spring equinox approaches. Suomi National Polar-orbiting Partnership (NPP) OMPS LP observations since 2012 show a relatively consistent seasonal pattern of PSC formation and evolution in the Southern Hemisphere, but significantly more variability during each season and between seasons in the Northern Hemisphere. Comparisons of OMPS LP PSC detections with concurrent Cloud-Aerosol Lidar with Orthogonal Polarization (CALIOP) observations show good agreement in spatial distribution and seasonal evolution when the CALIOP latitude coverage is screened to the range viewed by OMPS LP daytime measurements. LP measurements from current and future Joint Polar Satellite System (JPSS) satellites will enable us to follow long-term changes in PSC behavior, such as possible effects of the increased stratospheric water vapor from the Hunga Tonga-Hunga Ha'apai eruption.

Plain Language Summary

Observations of polar stratospheric clouds (PSCs) provide information about the possible magnitude of springtime polar ozone depletion. Ozone Mapping and Profiler Suite (OMPS) Limb Profiler (LP) measurements can identify PSCs and track their seasonal evolution. OMPS LP observations since 2012 show significantly more variability between different years in the Northern Hemisphere compared to the Southern Hemisphere. Continued OMPS LP measurements in the future can monitor long-term changes in PSC behavior.

1. Introduction

The stratospheric ozone layer in the Southern Hemisphere (SH) polar region typically experiences significant depletion during late winter and early spring (August-October). A key element in this process is the heterogeneous chemistry of chlorine reservoir species on polar stratospheric clouds (PSCs) during polar night releasing chlorine gas (Solomon, 1999). The return of sunlight in the spring photolyzes the chlorine gas, initiating a catalytic reaction that leads to rapid ozone destruction. PSCs fall into three classes, with different existence temperature thresholds: nitric acid trihydrate (NAT) particles, also known as Type Ia; liquid supercooled ternary solution (STS) droplets, also known as Type Ib; and water ice particles, also known as Type II (Tritscher et al., 2021). Of the three types, NAT particles typically have the highest existence temperature ($T_{NAT} \approx$ 193 K), followed by STS particles ($T_{STS} \approx 189$ K) and then ice particles ($T_{ice} \approx 187$ K). Although the density of NAT particles can be low, these particles can grow to relatively large size (Molleker et al., 2014), and settle more rapidly than other particles, removing HNO_3 and denitrifying the polar vortex (e.g., Solomon, 1999; Waibel et al., 1999).

Northern Hemisphere (NH) seasonal ozone depletion is normally less severe than in the SH, and the NH interannual variability in depletion is large because the NH polar vortex is frequently disrupted by planetary waves (e.g. Waugh et al., 2017). This disruption of the NH vortex generally warms the vortex above PSC existence temperatures, although PSC's will form where temperatures are suppressed by mountain waves. The dynamics of the active Arctic vortex reduces the chemical isolation of the region. Unless there is a major stratospheric warming in late January, the Arctic vortex reaches minimum temperatures in late winter. Observations of NH PSCs in late winter and early spring thus provide valuable precursor information for prediction of springtime NH ozone depletion.

The Ozone Mapping and Profiler Suite (OMPS) Limb Profiler (LP) is a hyperspectral instrument designed to make limb scattering measurements of ozone (Kramarova et al., 2018) and stratospheric aerosols (Taha et al., 2021). It uses a 2-D charge-coupled device (CCD) detector that simultaneously views the atmosphere over the altitude range 0-80 km with 1 km vertical sampling and the spectral range 290-1000 nm. The spectral resolution is variable ($\Delta\lambda$ = 1-20 nm). Jaross et al. (2014) describes the LP instrument in more detail. OMPS LP views backwards along the satellite orbit track with three parallel slits, one aligned with the satellite path and the other two oriented 4.25° to each side of this path, which gives a cross-track separation between radiance profiles of ~250 km at the tangent point. The along-track horizontal resolution of OMPS LP is approximately 120 km for a 1 km vertical sample size. The cross-track horizontal sample size is 2.2 km for a slit width of 0.6 mrad. The first LP instrument was launched on the Suomi National Polar-orbiting Partnership (S-NPP) satellite in October 2011, and a second LP instrument was launched on the NOAA-21 satellite in November 2022. Both satellites are in sun-synchronous orbits with an ascending node equator-crossing time of 1330. The LP sampling interval for S-NPP is 18.7 seconds, which gives an along-track profile spacing of approximately 120 km. The LP sampling interval on NOAA-21 was set to 15 seconds (96 km profile spacing) at launch, but was reduced to 7.5 seconds (48 km profile spacing) in December 2023.

The NASA operational algorithms for retrieving LP ozone and aerosol products need to identify the presence of clouds to establish a lower boundary for the retrieval, since the radiance signal can saturate at low altitudes. Chen et al. (2016) developed a cloud top detection algorithm for LP measurements that utilizes the radiance ratio, R(z), the vertical gradient of the $\log_e$ color ratio profile CR(z). The color ratio is defined as the radiance at 675 nm divided by the radiance at 869 nm.

$$ln\ R(z) = \frac{\partial}{\partial z} ln\ [CR(z)] \qquad [1]$$

They found that setting a fixed threshold of $ln(R) = 0.15$ for this quantity provided cloud detection results that agreed well with concurrent Cloud-Aerosol Lidar with Orthogonal Polarization (CALIOP) observations over a four-year analysis period.

DeLand et al. (2020) developed an approach to identify PSCs within the LP cloud detection data set based on the reported altitude and background atmosphere temperature. In this paper, we present an updated version of this algorithm that improves the reliability of the PSC detections, and discuss results obtained from 12 years of S-NPP OMPS LP observations. We validate our OMPS LP PSC product using comparisons to concurrent measurements from the CALIOP

instrument flying on the Cloud-Aerosol Lidar and Infrared Pathfinder Satellite Observations (CALIPSO) satellite. CALIOP operated at 532 nm and 1064 nm, creating profiles of backscattered signal with high vertical resolution and spatial sampling (Winker et al., 2009). Only nighttime observations were used for PSC detection to take advantage of reduced background noise from scattered sunlight. The polarization sensitivity of CALIOP provided valuable insight into the particle shape and composition of PSCs. Pitts et al. (2018) gives a thorough description of the CALIOP PSC detection algorithm and results.

2. PSC Detection Algorithm

Our data source is the NASA OMPS LP V2.1 aerosol daily product described by Taha et al. (2021). In addition to radiance profiles and aerosol extinction coefficient profiles at multiple wavelengths, this data product includes co-located ancillary meteorological data (specifically, temperature profiles and tropopause height) taken from NASA GSFC Global Modeling Assimilation Office (GMAO) Forward Processing for Instrument Team (FP-IT) data (Gelaro et al., 2017) that support our analysis. All LP profile quantities are reported on an altitude grid with 1 km spacing. We consider the altitude range 8.5-34.5 km and the latitude range 50°-90° for our PSC analysis. We first extract the radiance ratio profile for each measurement, and search for a maximum value that exceeds the cloud detection threshold of $ln(R) = 0.15$. We also require any detection to be at least 2 km above the local Modern Era Retrospective analysis for Research and Applications, Version 2 (MERRA-2) tropopause (Gelaro et al., 2017) to filter out cirrus clouds.

LP radiance measurements can experience transient events due to charged particle impacts on the CCD, particularly when the satellite flies through the South Atlantic Anomaly. These events can produce a sharp increase in radiance for a single wavelength and altitude, thus creating false cloud detections in the radiance ratio profile. We therefore apply the following tests to ensure that all possible PSC detections are valid.

1. The aerosol scattering index (ASI) at 869 nm must be greater than ASI(675 nm) at cloud altitude to satisfy the expected spectral dependence. (ASI is the difference between observed radiance and calculated Rayleigh scattering radiance, both normalized at 38.5 km)
2. The ASI at 675 nm and cloud altitude must exceed the noise threshold for successful aerosol retrieval, $ASI(675, z_{cloud}) > 0.05$.
3. The 869 nm extinction coefficient at cloud altitude must be greater than our assumed aerosol retrieval detection threshold of 1.0×10^{-5} km^{-1}.

While these tests are effective for identifying PSC events, the LP radiance ratio method will also flag the presence of dense aerosol layers, such as those produced by volcanic eruptions or pyrocumulonimbus plumes. We therefore use the term “high clouds” for all events examined in this paper, while noting that some situations may have a higher fraction of non-PSC events. We discuss our capability to distinguish between different event types in a later section.

Once a potential high cloud or thick aerosol layer has been identified, classification as a PSC requires the background temperature at cloud height to be lower than the nitric acid trihydrate (NAT) existence temperature (T_{NAT}) as defined by Hanson and Mauersberger (1988). We use concurrent Aura Microwave Limb Sounder (MLS) V5 H_2O (Lambert et al., 2007; Livesey et al.,

2022) and HNO_3 (Santee et al., 2007; Livesey et al., 2022) profiles to calculate $T_{NAT}(z)$ for each LP measurement. This calculation will produce a low biased temperature $T_{NAT}(z)$, since both H_2O and HNO_3 may also be sequestered on particles and thus not fully represented in the MLS gas phase profiles. We discuss this situation further in Section 3.2. The nearest MLS daytime measurement is selected, with a maximum separation of 1000 km. If no MLS data are available within this separation distance, we use H_2O and HNO_3 MLS climatological profiles based on typical seasonal average data for polar winter and spring (DeLand et al., 2020). We typically find that no more than 2-3% of our samples require the use of the climatological profiles described previously based on this geographical test.

3.0 Results

In the sections below we show typical PSC detection algorithm results as daily maps, validation from coincident measurements, seasonal statistics, color ratio analysis, and seasonal and annual variations in PSC area.

3.1 Daily Maps

Figure 1(a) shows a typical OMPS LP daily map of high cloud and PSC location and altitude in the Southern Hemisphere on August 9, 2016. The dashed black line shows the maximum latitude viewed by OMPS LP on this date, since OMPS LP only measures in daytime. In this SH example, 87 of the 93 candidates pass the PSC detection test. Cloud altitudes vary from 18.5 km to 25.5 km. The identified PSCs are all located at longitudes between 0°E and 180°E. The regional character of the PSC distribution is consistent with previous results from the CALIOP lidar on the Cloud-Aerosol Lidar and Infrared Pathfinder Satellite Observations (CALIPSO) satellite (Pitts et al., 2018).

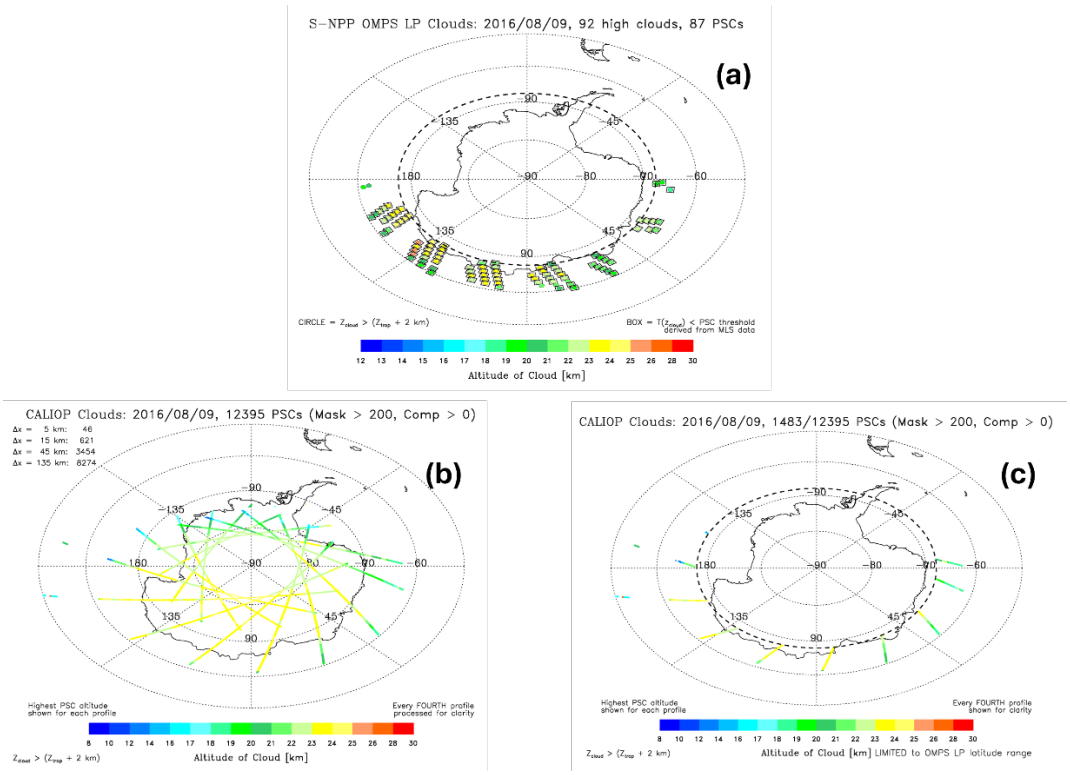

Figure 1. (a) OMPS LP high cloud and polar stratospheric cloud detection between 50°S and 90°S for August 9, 2016. Circles indicate all "high" clouds as defined in the text. Squares indicate clouds whose background temperature is below the T_{NAT} threshold. Black dashed line indicates the maximum latitude of solar illumination on this date. (b) CALIOP PSC detections between 50°S and 90°S for August 9, 2016. Colors indicate the highest PSC detection for an individual profile. Only every fourth profile is shown for clarity. The legend indicates the number of PSC detections within each horizontal averaging interval (see text). (c) CALIOP PSC detections for August 9, 2016, with latitude sampling limited to the maximum poleward value observed by OMPS LP (dashed line).

Figure 1(b) shows the distribution of all PSC detections from CALIOP measurements for the same date. The colors represent the highest PSC altitude for each profile to be consistent with the OMPS LP detection method, although a single CALIOP profile may have dozens of layers. Cloud mask values for any cloud above the tropopause are included in the CALIOP data set, but the clouds shown in Figure 1(b) are also required to have $z_{PSC} > (z_{tropopause} + 2\ km)$ for consistency with our OMPS LP approach. The CALIOP PSC feature mask also contains information about the horizontal averaging interval used for each detection. For this date, approximately 2/3rds (66.8%) of the PSC detections use the longest averaging interval (Δx = 135 km), a value which is comparable to the horizontal averaging of OMPS LP at 1 km vertical sampling. The overall distribution of PSC locations suggests that the coldest temperature region is offset from the South Pole. Figure 1(c) shows the CALIOP PSC detections for the same date when the latitude range is restricted to the OMPS LP sampling range. Only 12% of the original detections are now available, and the geographic distribution is consistent with the OMPS LP map shown in Figure 1(a).

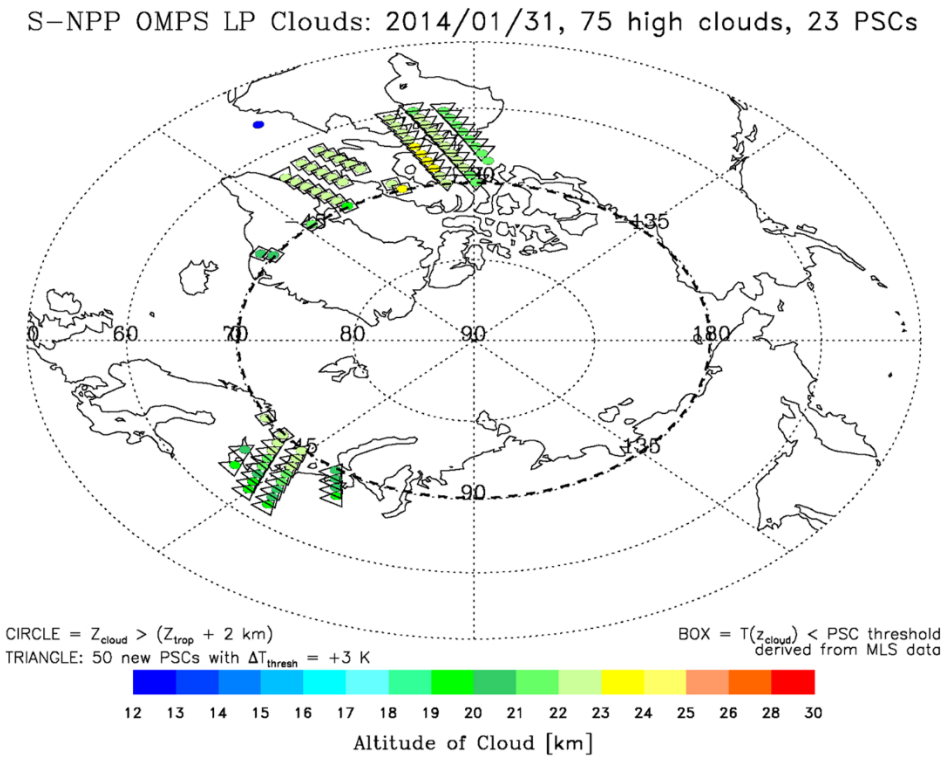

Figure 2. OMPS LP high cloud and polar stratospheric cloud detection between 50°N and 90°N for January 31, 2014. Identifications are as in Figure 1(a). Triangles indicate "high" clouds whose background temperature is within +3 K of the T_{NAT} threshold, as discussed in the text.

Figure 2 shows an OMPS LP map of high clouds in the Northern Hemisphere for January 31, 2014. The cloud locations are confined to three geographic clusters with limited longitudinal extent, as with the SH (Figure 1(a)). The CALIOP PSC detections for the same date (not shown) have clusters of clouds in the same locations when the OMPS LP latitude sampling is used, as well as additional detections between 45°E and 45°W longitude that occur poleward of the OMPS LP sampling limit. We note that most of the clouds in two of the three clusters do not pass the $T_{cloud} < T_{NAT}$ PSC detection threshold test, resulting in only 23 nominal PSC detections from 75 events. However, the GEOS FP-IT temperature data used by our PSC algorithm may not capture local fluctuations caused by orographically and convectively generated gravity waves that can locally lower the temperature (Orr et a., 2020; Weimer et al. 2021). In the case shown here, lowering the background temperature by 3 K - a value that encompasses balloon observed gravity wave temperature fluctuations (Schoeberl et al., 2017) - results in 50 additional PSC detections (shown by triangles) that give a more complete PSC field within the high cloud field. We discuss this result further in the next section.

3.2 Coincident Measurement Validation

The dense spatial sampling of both OMPS LP and CALIOP makes it possible to perform coincidence analysis on individual days to help validate the LP PSC results. We chose a maximum

separation of 200 km between the LP tangent point and CALIOP profile location for the results shown here, since this is consistent with the typical horizontal averaging for both instruments. We do not impose a minimum time difference requirement because the OMPS LP daytime measurements and the CALIOP PSC product (night measurements only) typically differ in sampling time by 9-10 hours.

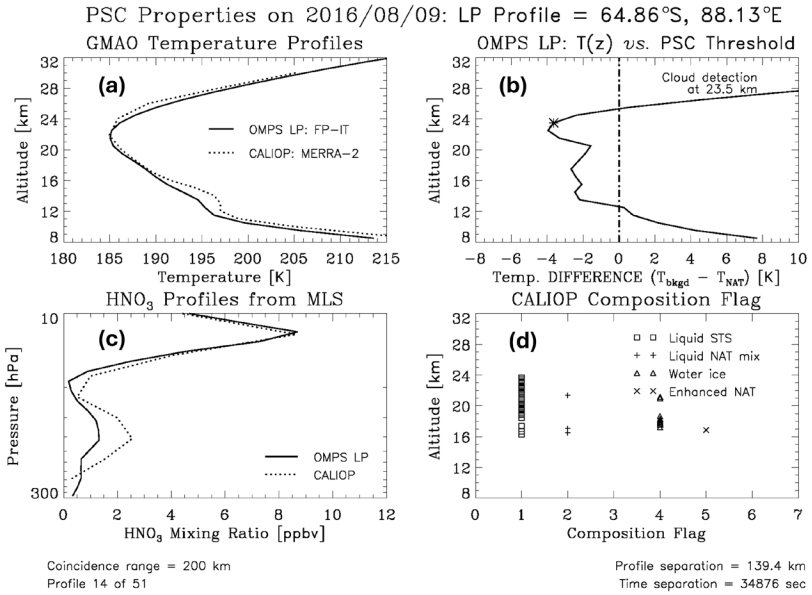

Figure 3. Coincidence analysis results for a selected OMPS LP event on August 9, 2016 where both CALIOP and OMPS LP identify a PSC. (a) Background temperature profiles for OMPS LP analysis (*solid*) and CALIOP PSC product (*dotted*). (b) Difference between OMPS LP background temperature and calculated NAT threshold temperature. *asterisk* = altitude of OMPS LP cloud detection. (c) HNO_3 mixing ratio profiles used for OMPS LP analysis (*solid*) and profiles used for the CALIOP PSC product (*dotted*). (d) Altitude distribution of CALIOP composition flag for PSC layers. *squares* = liquid STS particles, *plusses* = liquid NAT mix, *triangles* = water ice, *crosses* = enhanced NAT particles.

Figure 3 shows an example of results from August 9, 2016, when 51 OMPS LP profiles containing high clouds had CALIOP profiles within 200 km. We show ancillary information in some panels of this figure because there are differences in the approaches used by the OMPS LP and CALIOP teams. For example, the OMPS LP analysis uses GMAO FP-IT temperature profiles interpolated to the time of the LP measurement, whereas the CALIOP PSC product reports a temperature profile from MERRA-2 re-analysis interpolated to the location of the CALIOP measurement (Figure 3(a)). The OMPS LP analysis uses the single HNO_3 profile closest to each LP event, whereas the CALIOP PSC product reports a HNO_3 profile interpolated along the MLS orbit track (which is aligned with the CALIPSO orbit) to the location of the CALIOP profile (Figure 3(c)).

Figure 3 illustrates an event where OMPS LP and CALIOP both detect a PSC. The OMPS LP detection occurs at an altitude of 23.5 km, and the LP background temperature stays below the NAT existence threshold ($T_{background} - T_{NAT} < 0$) down to ~14 km (Figure 3(b)). The CALIOP PSC

composition flag indicates that liquid STS particles are present throughout this column, with examples of other particles (liquid NAT mix, water ice, enhanced NAT) at lower altitudes (Figure 3(d)).

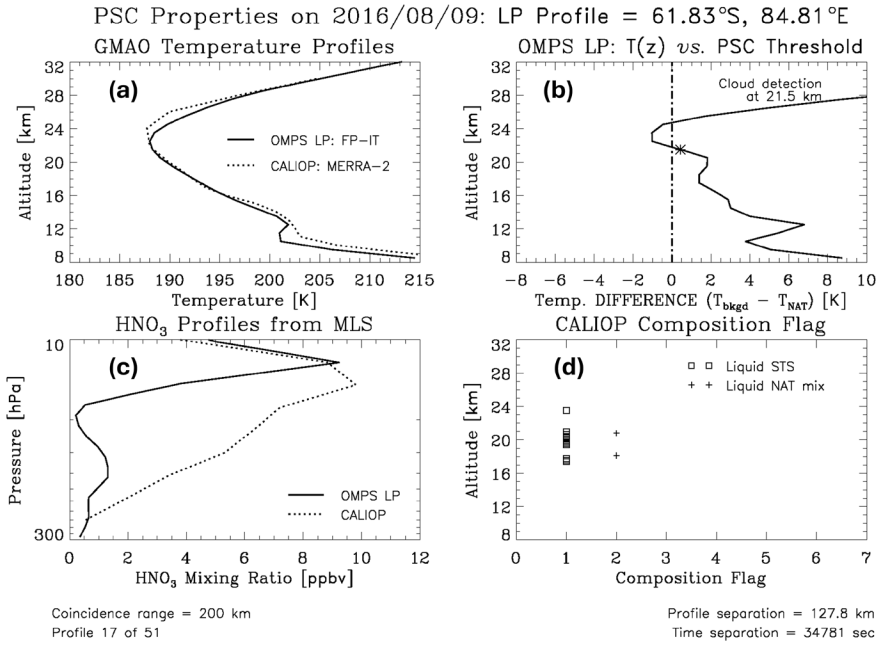

Figure 4. Coincidence analysis results for a selected OMPS LP event on August 9, 2016 where CALIOP identifies a PSC, but OMPS LP does not identify a PSC. Panel identifications are as in Figure 3.

Figure 4 shows a similar analysis for a nearby LP event (latitude difference = 3.0°, longitude difference = 3.3°) on the same date. The CALIOP composition flag shows predominantly liquid STS particles (Figure 4(d)). This is a consistent feature for most LP PSC detections in the Southern Hemisphere. However, the LP cloud detection at 21.5 km has a background temperature that is 0.4 K above the calculated NAT threshold (Figure 4(b)). For this event, the LP analysis selected the same MLS HNO_3 profile shown in Figure 3(c), whereas the interpolated HNO_3 profile created for the CALIOP PSC product shows significantly larger values at 20-24 km. This result suggests that the LP analysis is using a specific profile where PSCs are sequestering HNO_3. The lower HNO_3 values assumed for the LP NAT threshold calculation will reduce $T_{NAT}(z)$ by 2-3 K in this altitude region, which leads to the non-detection of a PSC in the LP analysis.

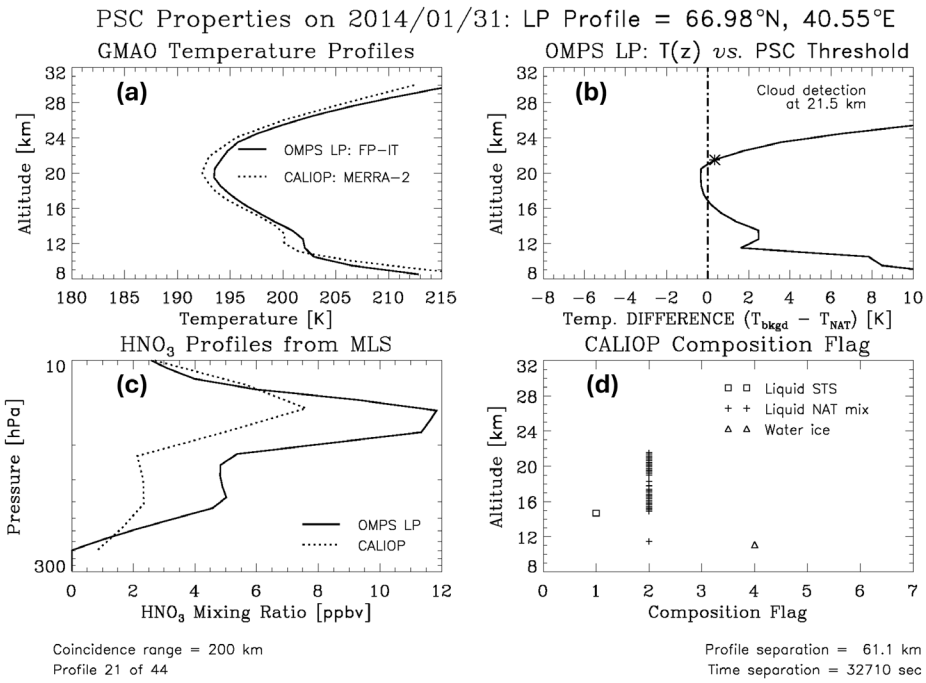

Figure 5. Coincidence analysis results for a selected OMPS LP event on January 31, 2014 where CALIOP identifies a PSC, but OMPS LP does not identify a PSC. Panel identifications are as in Figure 3.

Figure 5 shows an example of coincidence analysis for the Northern Hemisphere on January 31, 2014. The LP profile location corresponds to one of the clusters in Figure 2 that show PSC identifications after shifting the LP background temperatures by -3 K. Figure 5(b) shows that the LP temperature at cloud height is only 0.2 K above the calculated NAT threshold, which is within the difference between the FP-IT and MERRA-2 temperature profiles (Figure 5(a)). Note that shifting the cloud altitude down by 1 km (the step size of LP altitude sampling) would also lower the background temperature enough to enable a PSC identification. The CALIOP composition flag is dominated by liquid NAT mix particles (Figure 5(d)), which is more common for LP events in the NH.

3.3 Seasonal Statistics

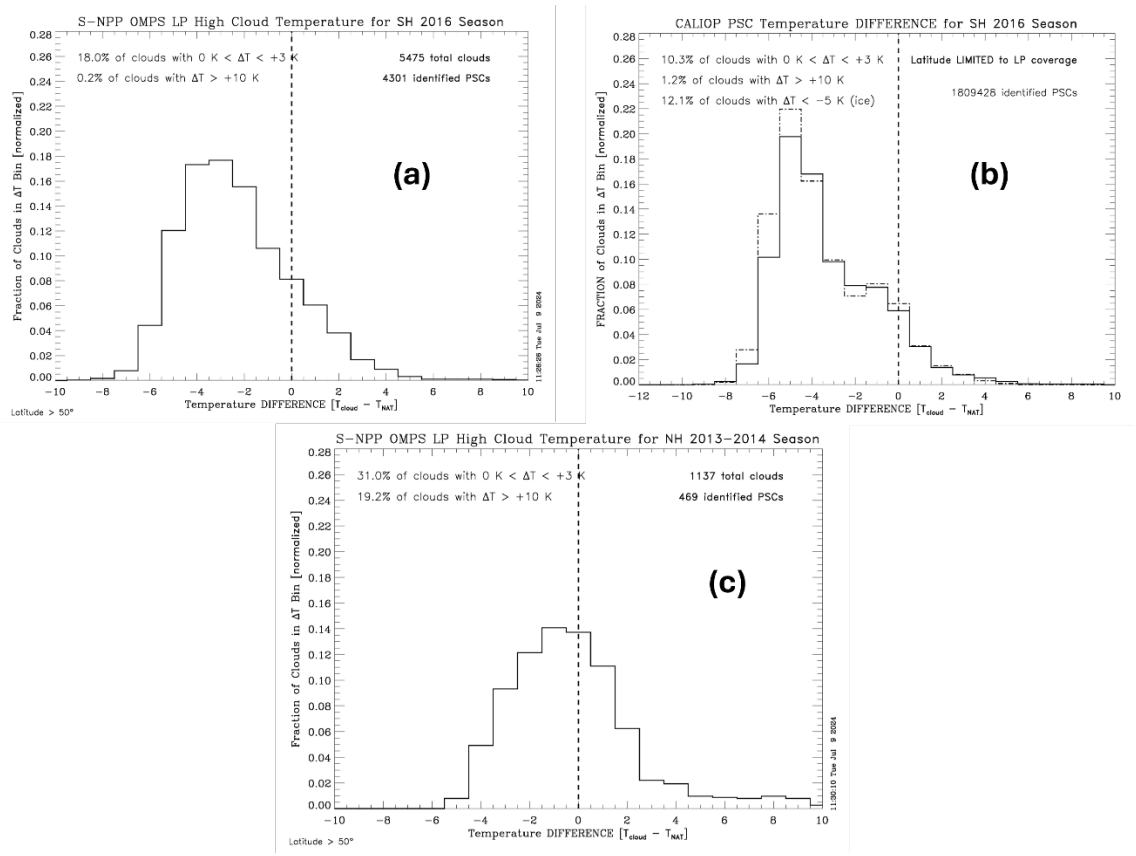

Figure 6. (*a*) Distribution of LP high cloud temperature difference values relative to T_{NAT} for the SH 2016 season. The vertical dashed line indicates zero difference. All values are normalized to the total number of high clouds. (*b*) Distribution of CALIOP PSC temperature difference values relative to T_{NAT} for the SH 2016 season. *Solid* = latitude range limited to OMPS LP sampling. *Dot-dashed* = Full CALIOP data set. (*c*) Distribution of LP high cloud temperature difference values relative to T_{NAT} for the NH 2013-2014 season.

We can examine the distribution of the temperature difference between high clouds and NAT threshold [$\Delta T_{cloud} = T_{cloud} - T_{NAT}$] to assess the frequency of the marginal cases that reduce OMPS LP PSC detection frequency. Figure 6(a) shows the normalized distribution of ΔT_{cloud} for all high clouds in the SH 2016 season, binned at 1 K steps. The maximum occurrence frequency is found at -3 K. Only 3.4% of the high clouds have $\Delta T_{cloud} > +3$ K, indicating that most high clouds identified by the algorithm are PSCs. Figure 6(b) shows the distribution of ΔT_{cloud} for CALIOP PSCs in the SH 2016 season, with latitudes limited to LP coverage for each day. This restriction only keeps ~5% of the total CALIOP detections, which is still a factor of 300 more than the OMPS LP total. The maximum occurrence frequency shifts to -5 K, but the overall shape of the distribution is very similar to the LP distribution in Figure 6(a). Note that the CALIOP distribution also has a small tail of values with $\Delta T_{cloud} > 0$. The dot-dashed line shows that the distribution using all CALIOP data is very similar.

Figure 6(c) shows the normalized distribution of ΔT_{cloud} for the NH 2013-2014 season. The maximum frequency is now found at -1 K. Only 41.2% of the high clouds are identified as PSCs, while an additional 31.0% have $\Delta T_{cloud} < +3$ K. In addition, there is a significant fraction of clouds with $\Delta T_{cloud} > +10$ K (19.2%) which are unlikely to be PSCs. This is a common occurrence for NH PSC seasons. Figure 7 shows an example of OMPS LP high cloud detections on 25 January 2018, with FP-IT temperature contours at 18.5 km (~70 hPa) overlaid. All of the PSCs (blue filled circles) and most of the additional high clouds (open circles) lie within the region encompassed by the 200 K temperature contour. In contrast, all cases with $\Delta T_{cloud} > +10$ K (red filled squares) are located in different regions with warmer background temperatures. The geographic separation from the vortex region strongly suggests that these detections represent aerosol layers, as we discuss below.

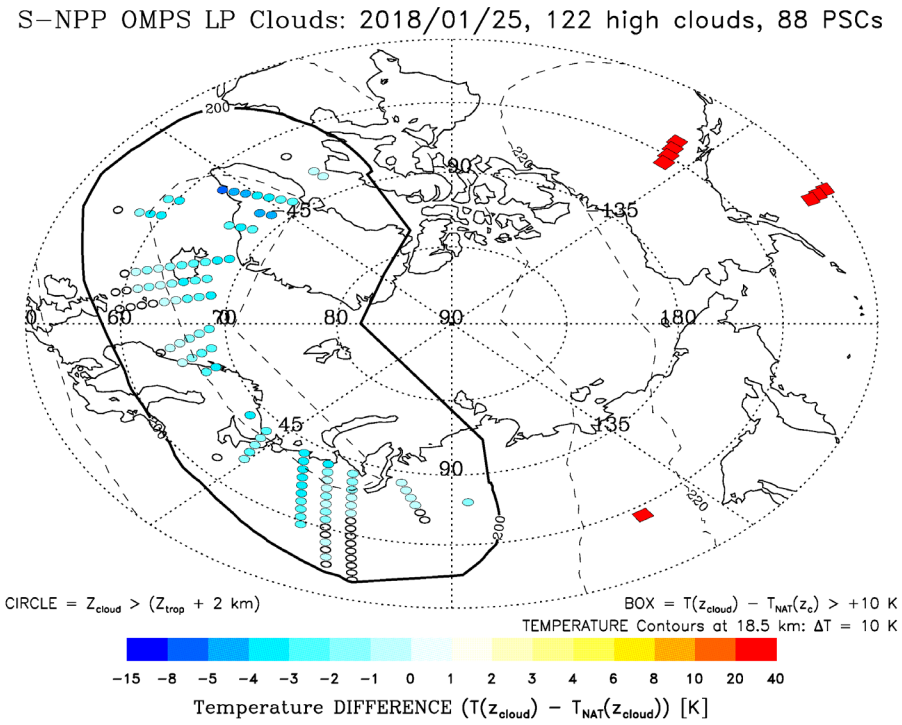

Figure 7. OMPS LP high cloud detections on January 25, 2018. *Blue filled circles* = PSC identifications. *Open circles* = High clouds with $\Delta T_{cloud} < +10$ K. *Red filled boxes* = High clouds with $\Delta T_{cloud} > +10$ K. *Contours* = FP-IT temperature at 18.5 km.

Tables 1 and 2 compile PSC classification and temperature difference statistics for all S-NPP OMPS LP seasons. SH seasons typically have less than 4% clouds with $T_{cloud} > (T_{NAT} + 3$ K), while NH seasons often have 30% or more clouds with $T_{cloud} > (T_{NAT} + 3$ K). Part of this persistent hemispheric difference can be attributed to colder synoptic temperatures in the SH. When model-based background temperatures are very close to T_{NAT} at the location of a possible PSC, as is more common in the NH, then small changes in either threshold parameter (e.g. FP-IT temperature not capturing wave activity, local depletion of HNO_3 reducing calculated T_{NAT}) can cause a cloud detection to fail the temperature test. In addition, OMPS LP measurements are more sensitive to aerosol signals in the NH polar latitudes because these measurements are made at forward

scattering angles (typically less than 50°), so that aerosol phase function values are 5-10 times larger than for comparable SH latitudes during winter and spring (Loughman et al., 2018). As a result, thin aerosol layers in the NH are more likely to be identified as possible clouds in regions that are too warm to support PSC formation. Note that there are many more high clouds identified when plumes from volcanic eruptions or extensive wildfires are present, such as following the Calbuco eruption (SH 2015), the Raikoke eruption and Siberian fires (NH 2019-2020), and the Hunga eruption (SH 2022; see Taha et al., 2022).

Season	Number of High Clouds	Number of PSCs	Fraction of PSCs	0 K < ΔT_{cloud} < +3 K	ΔT_{cloud} > +10 K
2012	3575	2900	81.1%	15.5%	0.3%
2013	3940	3248	82.4%	14.7%	0.3%
2014	4603	3498	76.0%	20.9%	0.1%
2015	12346	8828	71.5%	18.2%	5.3%
2016	5475	4301	78.6%	18.0%	0.2%
2017	2740	2203	80.4%	16.4%	0.5%
2018	6657	5338	80.2%	17.8%	0.1%
2019	4779	3521	73.7%	22.0%	0.3%
2020	7263	6157	84.8%	13.3%	0.2%
2021	5629	4804	85.3%	12.8%	0.0%
2022	13274	6068	45.7%	9.9%	27.9%
2023	7490	6004	80.2%	15.5%	0.4%

Table 1. S-NPP OMPS LP SH high cloud detection, PSC classification, and temperature difference statistics for all Southern Hemisphere seasons from 2012 through 2023. Results for +3 K < ΔT_{cloud} < +10 K have been omitted for clarity.

Season	Number of High Clouds	Number of PSCs	Fraction of PSCs	0 K < ΔT_{cloud} < +3 K	ΔT_{cloud} > +10 K
2012-2013	1383	491	35.5%	37.0%	23.9%
2013-2014	1138	469	41.2%	31.1%	19.2%
2014-2015	795	117	14.7%	12.7%	54.6%
2015-2016	3325	1554	46.7%	33.9%	6.2%
2016-2017	1158	326	28.2%	35.9%	17.3%
2017-2018	3595	1388	38.6%	35.0%	15.0%
2018-2019	647	122	18.9%	23.6%	46.8%
2019-2020	24364	6784	27.8%	24.9%	11.2%
2020-2021	1051	353	33.6%	23.3%	33.9%
2021-2022	4438	1459	32.9%	21.7%	38.7%
2022-2023	10687	1332	12.5%	18.4%	42.1%
2023-2024	11065	1153	10.4%	12.2%	58.4%

Table 2. S-NPP OMPS LP NH high cloud detection, PSC classification, and temperature difference statistics for all Northern Hemisphere seasons from 2012-2013 through 2023-2024. Results for +3 K < ΔT_{cloud} < +10 K have been omitted for clarity.

3.4 Color Ratio Analysis

The hyperspectral character of the OMPS LP measurements provides the opportunity to evaluate whether extinction color ratio values can be used to discriminate between Type Ia (NAT) and Type Ib (STS) PSCs. Color ratio analysis has been used to distinguish clouds from aerosols in Stratospheric Aerosol and Gas Experiment data (Thomason and Vernier, 2013; Schoeberl et al., 2021). We use LP extinction values at 509 nm and 869 nm for this analysis, since LP 997 nm measurements were not available for the first two years of the S-NPP mission. We also screen the measurements for a valid 509 nm extinction value at the cloud altitude.

Following the approach of Poole et al. (2003), we first determined a typical profile of 869 nm extinction background values (no PSC detection) from SH data over a potential temperature range of θ = 400-700 K. We then calculate the ratio of the observed and background 869 nm extinction [$Ext_{obs}(869)/Ext_{bkgd}(869)$] at the cloud height, and plot this ratio against the color ratio defined by Ext(509)/Ext(869) at the same altitude.

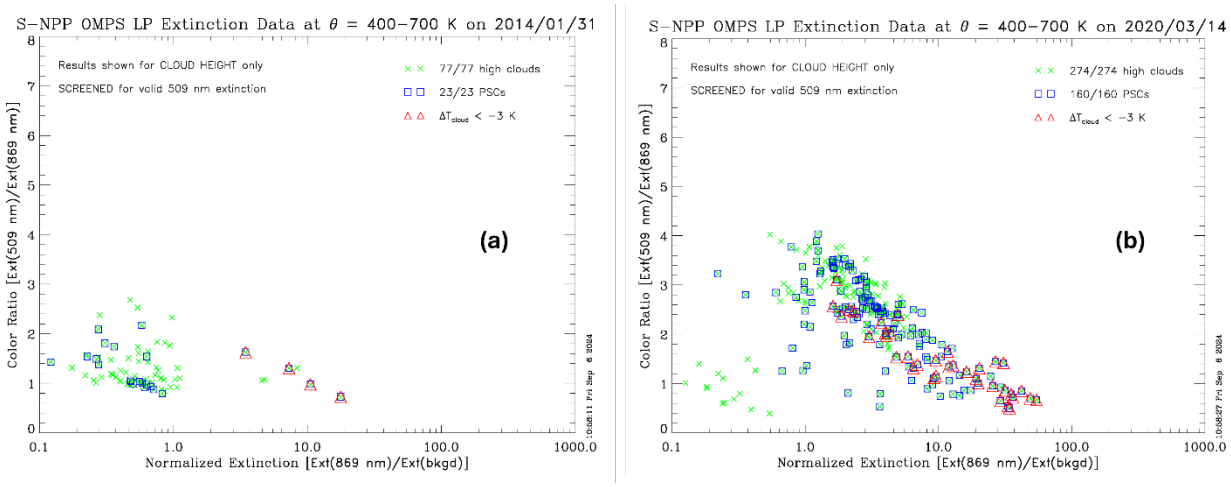

Figure 8. (a) OMPS LP NH color ratio (Ext(509 nm)/Ext(869 nm)) *vs*. normalized extinction at 869 nm for high cloud detections on January 31, 2014. *Green crosses* = high clouds, *blue squares* = identified PSCs, *red triangles* = temperature difference ($T_{cloud} - T_{NAT}$) < -3 K. The legend numbers for high clouds and PSCs indicate the number of cases with valid Ext(509 nm) compared to the total number of cases. (b) OMPS LP color ratio *vs*. normalized extinction for high cloud detections on March 14, 2020. Identifications are as in part (a).

Figure 8(a) shows these results for all OMPS LP high clouds observed on January 31, 2014, the date shown in Figure 2. Nominal PSCs (ΔT_{cloud} < 0 K) are identified with squares. A triangle is added for samples where ΔT_{cloud} < -3 K, which is approximately the point at which STS extinction

should begin to increase (Carslaw et al., 1999). These potential Type Ib samples also have higher normalized extinction values than other clouds, consistent with Figure 2 of Poole et al. (2003), although the numerical values shown here are probably different because of changes in wavelength selection. Figure 8(b) shows a similar analysis for March 14, 2020, during the very active NH 2019-2020 PSC season. Potential STS samples again show the highest normalized extinction values, although the separation from other samples is not as evident. The normalized extinction values consistently increase in magnitude with higher color ratio values.

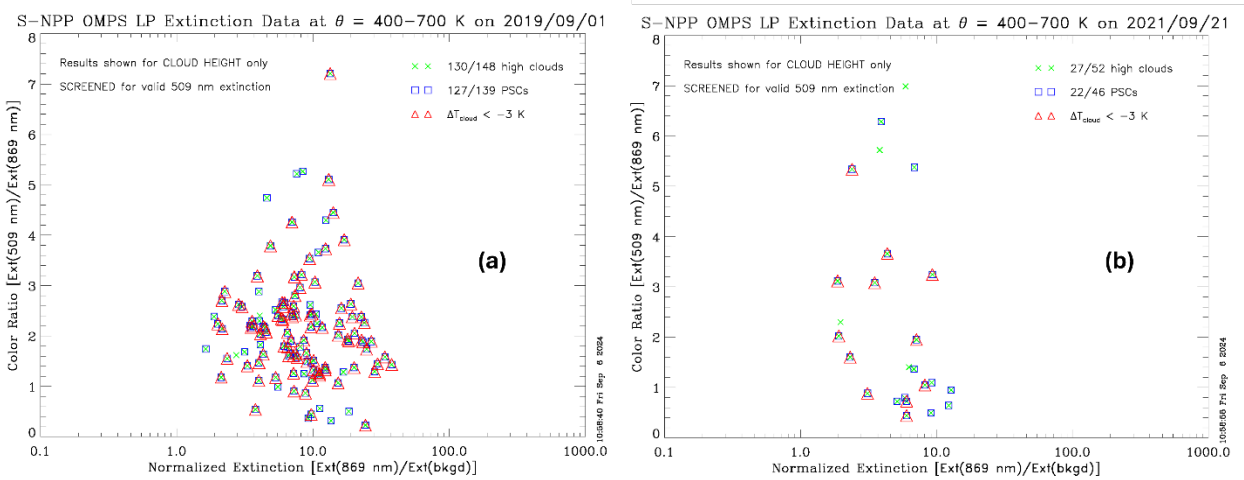

Figure 9. (a) OMPS LP SH color ratio (Ext(509 nm)/Ext(869 nm)) *vs*. normalized extinction for high cloud detections on September 1, 2019. *Green crosses* = high clouds, *blue squares* = identified PSCs, *red triangles* = temperature difference ($T_{cloud} - T_{NAT}$) < -3 K. The legend numbers for high clouds and PSCs indicate the number of cases with valid Ext(509 nm) compared to the total number of cases. (b) OMPS LP color ratio *vs*. normalized extinction for high cloud detections on September 21, 2021. Identifications are as in part (a).

Figure 9(a) shows the same LP color ratio analysis for a date in the SH 2019 PSC season (September 1, 2019). Almost all high clouds are identified as PSCs (as noted previously for SH measurements), and most also have ΔT_{cloud} < -3 K. However, the normalized extinction values do not show a systematic increase as the color ratio value changes. In addition, some high cloud samples were rejected for this analysis because no valid 509 nm extinction value was available at cloud altitude. This result is in part a consequence of the OMPS LP viewing geometry, which gives relatively high scattering angle values (θ = 140°-160°) for typical SH PSC observations. The corresponding aerosol signal can be very small because the phase function is low, and the extinction retrieval does not occur if the estimated aerosol signal is less than 1% of the calculated background signal with no aerosol present (Taha et al., 2021). Even when the 509 nm retrieval is possible, there may be Rayleigh scattering contamination in the result. Note that OMPS LP measurements of NH PSCs occur at much lower scattering angles (θ = 20°-40°), so the phase function and corresponding aerosol signal are much larger.

Figure 9(b) shows a similar analysis for a date in the SH 2021 PSC season (September 21, 2021). Almost half of the initial high cloud detections do not have valid 509 nm extinction data available.

The samples that are available again show no systematic variation in normalized 869 nm extinction with color ratio. While the results of applying color ratio analysis to OMPS LP data support the classification of Type Ib PSCs using ΔT_{cloud} values, they do not appear to be robust enough to be used independently for this purpose.

3.5 Seasonal and Interseasonal Changes in PSC Area

Understanding the area covered by PSCs at each altitude is an important element in estimating the potential magnitude of seasonal stratospheric chemical processing by PSCs, which is related to the ozone loss. DeLand et al. (2020) noted that since the OMPS LP cloud top algorithm only identifies the top of a PSC, an indirect approach is needed to estimate the depth of a cloud layer. They examined the extent of the region below each cloud where $T_{cloud} < T_{NAT}$, and included those layers in the calculation of total PSC area. While some cases can have layers up to 13 km in depth that satisfy this requirement, DeLand et al. (2020) found that limiting the layer depth to a maximum of 7 km below the cloud gave reasonable agreement with concurrent CALIOP data (Pitts et al., 2018) for selected dates. PSC area at each altitude is calculated as the product of the daily occurrence frequency in small latitude bands (3°-4°) and the spatial area of each band.

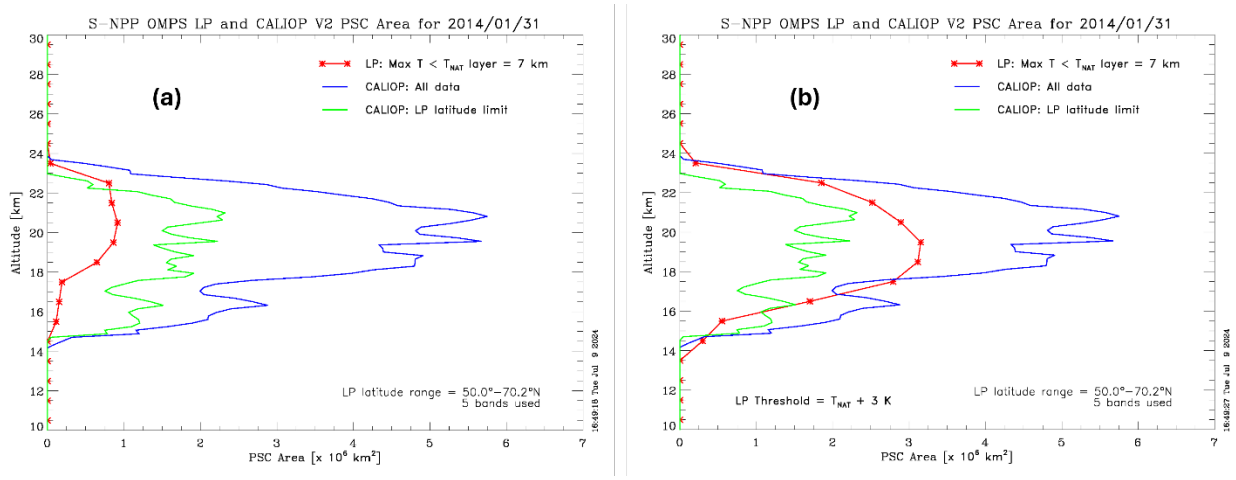

Figure 10. (a) PSC area (in 10^6 km^2) as a function of altitude for January 31, 2014. *Red* = OMPS LP, including all layers with $T < T_{NAT}$ up to 7 km below the cloud detection altitude. *Blue* = CALIOP area using all measurements. *Green* = CALIOP area limited to OMPS LP sampling region. (b) *Red* = OMPS LP area when the LP background temperatures are reduced by 3 K. *Green, blue* = same curves as in part (a).

Figure 10(a) shows an example of cumulative PSC area profiles for a single day (January 31, 2014). The LP results indicate that most nominal PSCs were identified at 22.5 km, consistent with the map shown in Figure 2. The CALIOP results show the presence of PSCs down to 14-15 km altitude, suggesting that the layer with $T_{cloud}(z) < T_{NAT}(z)$ could be as deep as 9 km. However, we found that increasing the maximum allowed LP layer depth to 9 km (or reducing it to 5 km) produced very little change, and only in the lowest portion of the LP area profile.

The CALIOP PSC area profile shown in Figure 10(a) is consistently larger than the LP area profile at all altitudes, even when the analysis region is limited to the LP latitude sampling. Figure 10(b) shows the change when the LP background temperatures are reduced by 3 K. The LP area profile is now greater than the CALIOP area profile (with restricted latitude coverage) at most altitudes as a result of increased PSC detections. Note that this result uses the same LP data shown in Figure 2, where the location of the clouds added by reducing the background temperature are geographically consistent with the original PSC detections. The additional clouds also increase the area at cloud top altitude. This increase in area represents a maximum change, since we do not have a way to independently evaluate the FP-IT temperatures to this level of accuracy. Nevertheless, it provides further evidence that small fluctuations in the FP-IT temperature fields, which affect the determination of PSC presence in LP measurements, are likely to be present in many cases. Underestimation of HNO_3 abundance due to the use of MLS data containing only gas phase information, which reduces the calculated T_{NAT} value and thus LP PSC identifications, can also lower the estimated LP PSC area.

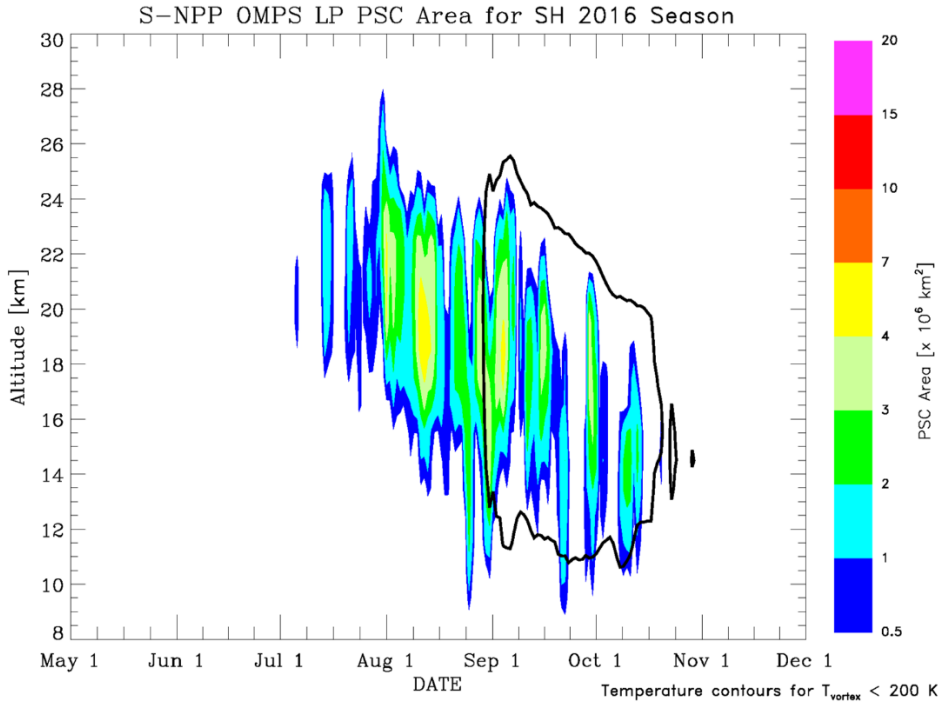

Figure 11. OMPS LP PSC area as a function of altitude during the SH 2016 season, including all layers with $T < T_{NAT}$ up to 7 km below the cloud detection altitude. Area values (in 10^6 km^2) are given by the color scale. *Black contours* = vortex-averaged temperature below 200 K, as defined in the text.

We can use these profiles to examine the evolution of PSC area during a full season, noting again that OMPS LP only samples the sunlit portion of the polar region. Figure 11 shows the evolution of the total PSC area viewed by S-NPP OMPS LP for the SH 2016 season. PSC detections begin at 24-25 km in mid-July, and gradually drop to 14-16 km by early October. PSC area typically increases as the altitude of the cloud tops decreases. The descent of the PSC peak area during the season is consistent with CALIOP observations, as reported by Pitts et al. (2018). This descent is

associated with cooling that begins at upper levels and progresses to lower levels (see Pitts et al. (2018), Figure 17). As particles settle, the upper levels denitrify and dehydrate, lowering the PSC formation temperature. Typically, around September 1, the upper vortex levels begin to warm.

We can verify this behavior by calculating the average FP-IT temperature profile within a polar vortex region for each day, defining the vortex region as any MLS observation where stratospheric column ozone < 170 Dobson units (DU). A 5-day smoothing is applied to the temperature data at each altitude to smooth day-to-day fluctuations in the averaged values. Figure 11 shows that the vortex-averaged temperature falls below 200 K between 12-25 km in late August, and stays below this threshold (with decreasing maximum altitude) until late October. This period coincides with the onset of maximum PSC activity (daily area > 2 x 10^6 km^2).

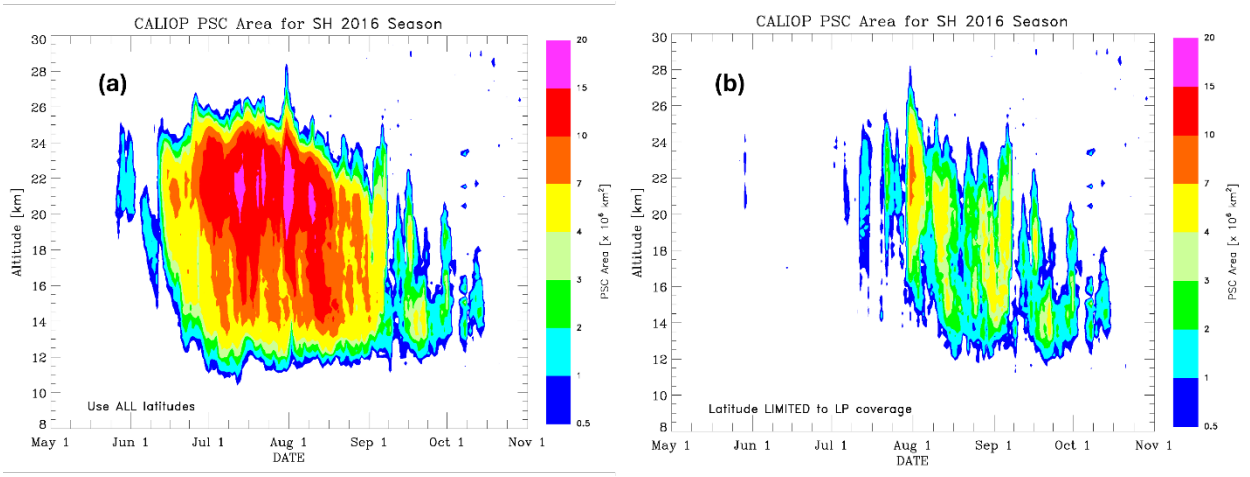

Figure 12. (a) CALIOP PSC area as a function of altitude during the SH 2016 season. Area values (in 10^6 km^2) are given by the color scale. (b) CALIOP PSC area for the SH 2016 season with daily latitude coverage limited to OMPS LP sampling.

Figure 12(a) shows the seasonal evolution of PSC area in CALIOP data for the SH 2016 season, using all observations. PSC detections begin in late May, and total area increases rapidly during June. Maximum areas exceeding 15 x 10^6 km^2 are observed during July and early August. Figure 12(b) shows the CALIOP PSC area time series for the SH 2016 season when the LP latitude sampling limit is applied. PSC detections are now sparse until the beginning of August, and the daily maximum area only briefly exceeds 7 x 10^6 km^2. It is clear that limiting the sampling region to the sunlit area observed by OMPS LP excludes the initial portion of the SH PSC season (solstice – 30 days to solstice + 30 days), where significant chlorine activation is occurring at high latitudes. The evolution of the PSC area in this figure from mid-July onward, where the maximum latitude sampled rapidly increases from 65° to 82°, is reasonably consistent with OMPS LP results.

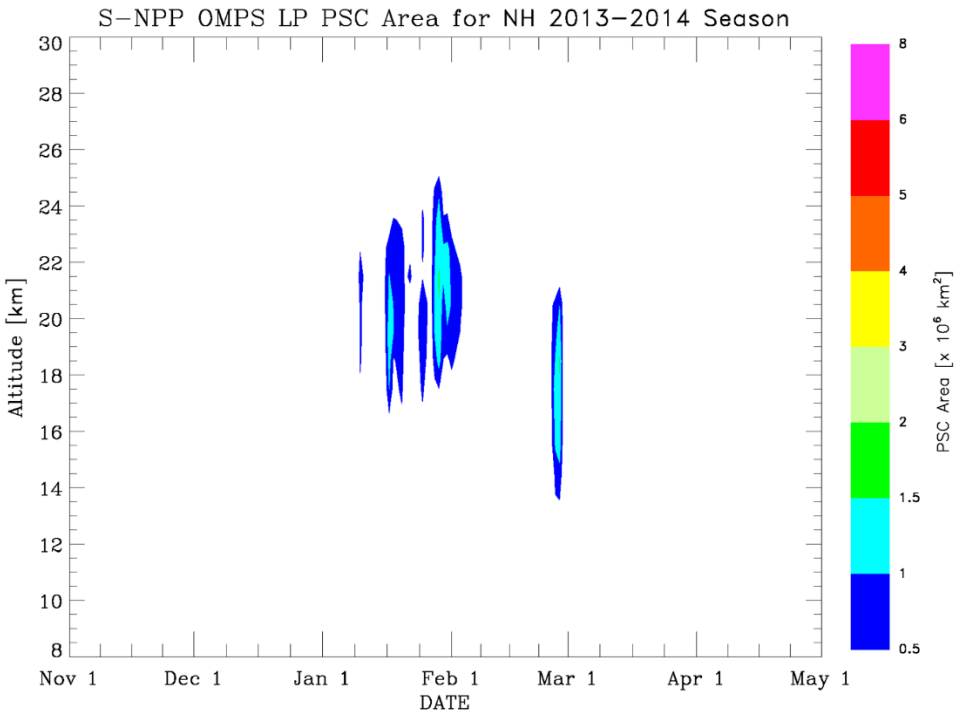

Figure 13. OMPS LP PSC area as a function of altitude during the NH 2013-2014 season. The color scale has been shifted compared to Figure 11.

Figure 13 shows the LP PSC area and vortex-averaged temperature time series for the NH 2013-2014 season. Note that the color scale has been revised for the lower PSC areas observed in the Northern Hemisphere. The stratospheric column ozone threshold value for the polar vortex definition has been raised to 220 DU for NH measurements. Even with this change, there are no intervals with average temperatures below 200 K. PSC occurrences cover a shorter period of the season compared to the SH example shown in Figure 11, with lower values for total area.

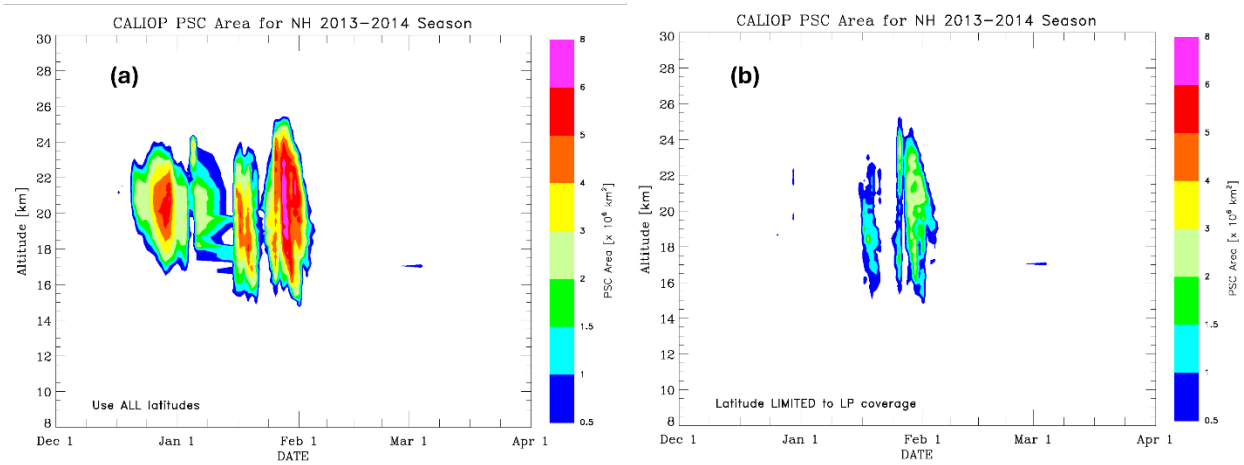

Figure 14. (a) CALIOP PSC area as a function of altitude during the NH 2013-2014 season. The color scale is consistent with Figure 13. (b) CALIOP PSC area

for the NH 2013-2014 season with daily latitude coverage limited to OMPS LP sampling.

Figure 14(a) shows the CALIOP PSC area time series for the NH 2013-2014 season using all measurements. Note that CALIOP NH PSC processing begins in December. There is a period of activity in late December that is not observed by OMPS LP, and maximum daily area values are 2-3 times larger than OMPS LP results. Note that CALIOP data are not available for February 21-28, 2014. Figure 14(b) shows the CALIOP PSC area time series for the same season when the LP latitude limit is applied. Similar to the changes observed in Figure 12(b) for SH measurements, there are very few PSCs detected prior to ~1 month after solstice, and the maximum daily area values are significantly reduced.

Figure 15 shows time series of daily LP PSC area for 12 SH seasons (2012 through 2023). PSC occurrence is typically intermittent before winter solstice, then becomes persistent by mid-July. Recall that OMPS LP can only make measurements in the sunlit portion of the vortex. Note that in some years PSC presence ends relatively early (e.g. SH 2013, SH 2019), while other years maintain cold temperatures and PSC formation into early November (e.g. SH 2015, SH 2020). Daily maximum PSC areas typically reach 4-6 x 10^6 km^2 in August-September. The SH 2023 season had an extended period of large PSC area values, which we discuss further below.

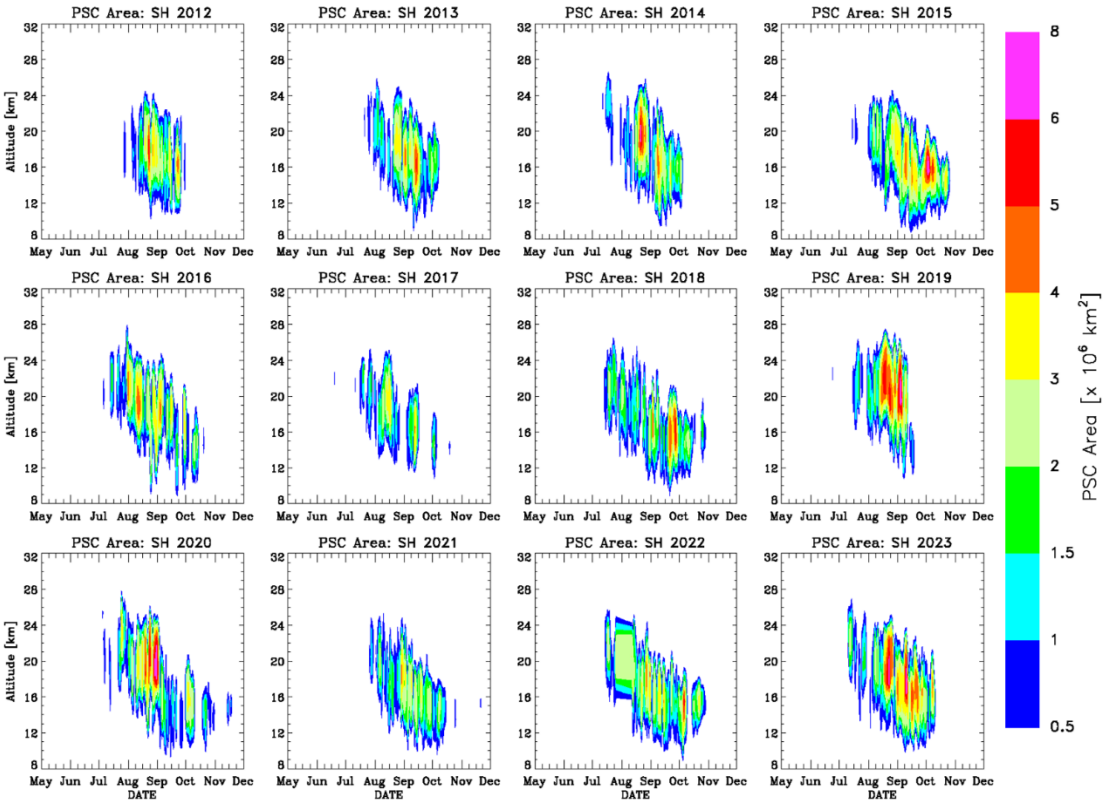

Figure 15. OMPS LP PSC area time series for Southern Hemisphere seasons from 2012 through 2023. Color scale is the same as shown in Figure 13.

Figure 16 shows time series of daily PSC area observed by OMPS LP for 12 NH seasons (2012-2013 through 2023-2024). PSC occurrence is sometimes observed in patches at 20-26 km prior to winter solstice (e.g. 2012, 2017, 2019). However, the duration of the season may only be ~2 months in the NH, and intervals with no PSCs often occur during the season. The magnitude of NH PSC area values is typically lower than observed in the SH, and more variable from season to season as noted previously (Pitts et al., 2018). The NH 2019-2020 season is notable in this regard for the magnitude and duration of PSC occurrence. LP PSC areas observed during March 2020 significantly exceed CALIOP PSC areas for the same month, which is an unexpected result. The low levels of wave activity in the NH 2019-2020 season led to a cold and long-lived vortex, with exceptional ozone losses in the lower stratosphere during April 2020 (e.g. Manney et al., 2020).

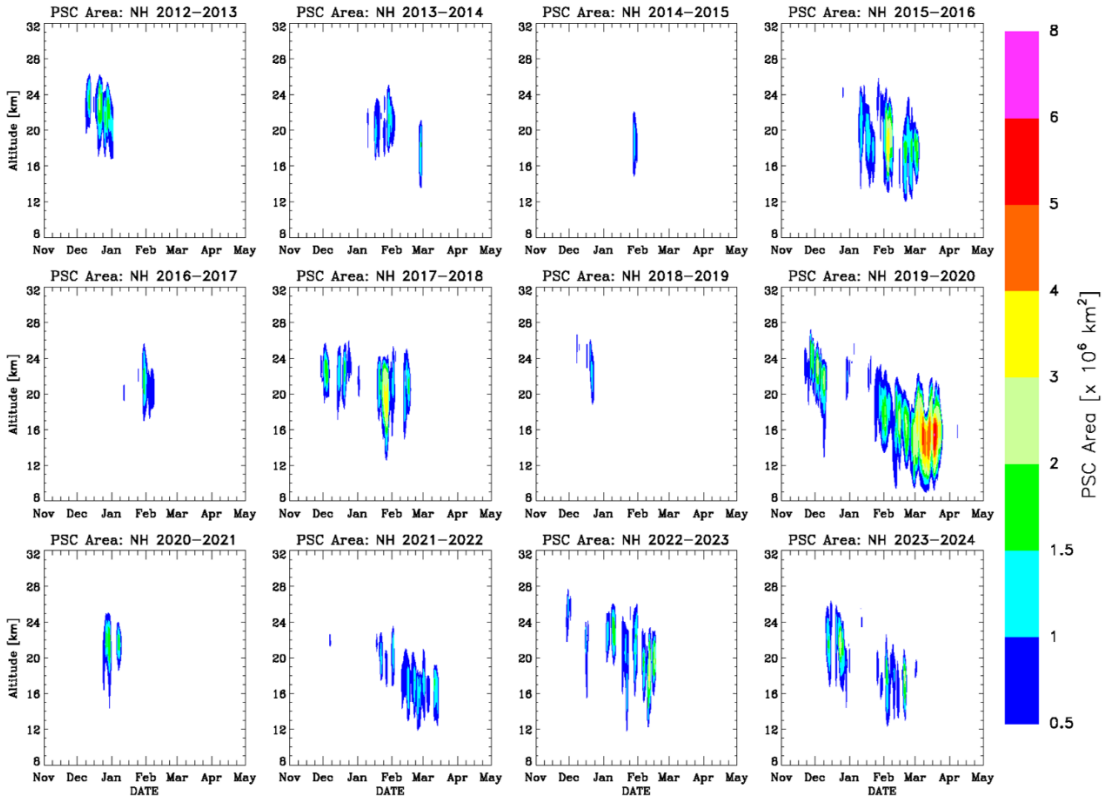

Figure 16. OMPS LP PSC area time series for Northern Hemisphere seasons from 2012-2013 through 2023-2024. Color scale is the same as shown in Figure 13.

A further illustration of how OMPS LP tracks the potential for springtime polar ozone depletion can be made by calculating the integrated volume of PSC occurrence (V_{PSC}) for each season. The standard definition of V_{PSC} (e.g. Rex et al., 2006; Strahan et al., 2016) utilizes the area inside the polar vortex that would support PSC existence (i.e. $T_{vortex} < T_{NAT}$) based on nominal profiles of H_2O and HNO_3. Since this definition includes large areas of polar night that OMPS LP does not see, we have calculated V_{PSC} using only the PSC areas shown in Figures 15 and 16, where T_{NAT} is typically determined using observed H_2O and HNO_3 profiles. The V_{PSC} results for all OMPS LP

seasons are shown in Figure 17. As expected, the V_{psc} integrated volume is lower than shown elsewhere (e.g. WMO(2022), Figure 4.2) because polar night regions are not considered. Note that the largest V_{PSC} value in the OMPS LP record is observed in the SH 2023 season, when residual stratospheric water vapor from the Hunga Tonga-Hunga Ha'apai eruption has been proposed to be present in the vortex region before large-scale dehydration began (Millán et al., 2024). NH V_{PSC} values are lower than all SH V_{PSC} values, with the notable exception of the NH 2019-2020 season. The PSC volume provides a qualitative measure for possible polar ozone depletion in late winter and early spring. In the Antarctic, all of the HCl is converted to active chlorine so the presence of PSCs after that conversion has completed does not increase ozone loss. This is not the case in the Arctic where PSCs are more intermittent as we have shown. Thus, there is a better correlation between Arctic PSC abundance and springtime ozone loss (e.g. 2016, 2018, 2020).

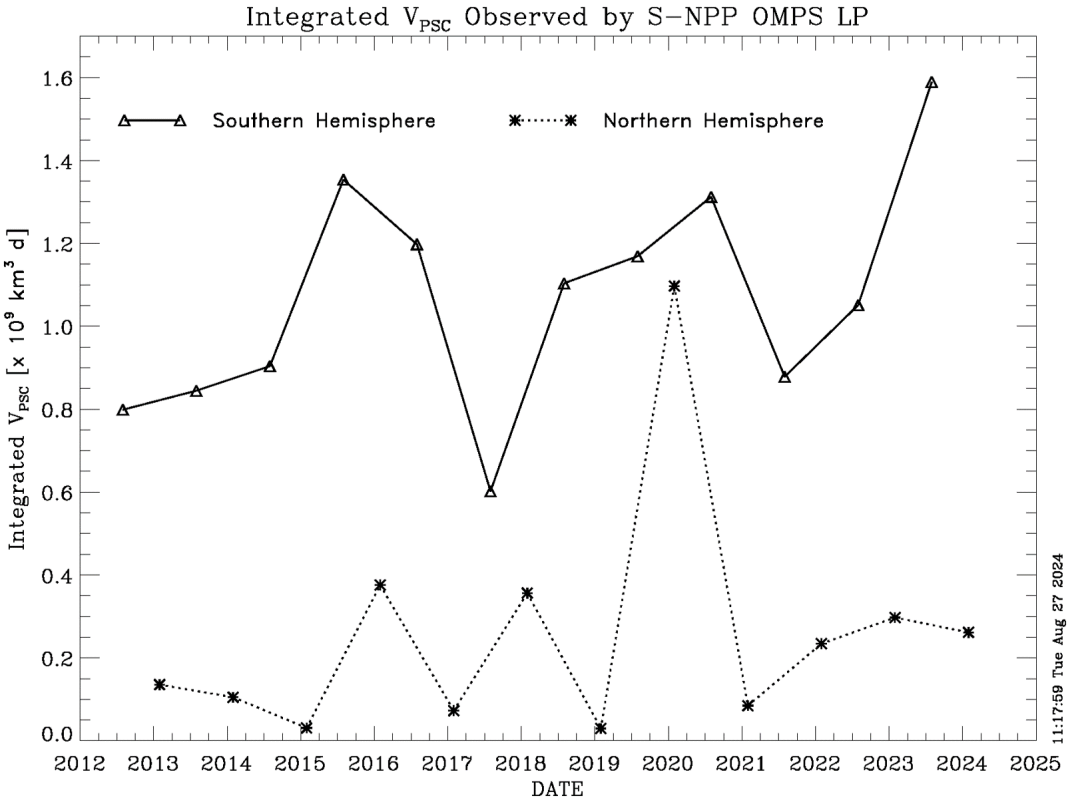

Figure 17. Integrated PSC volume (V_{PSC}) for regions observed by S-NPP OMPS LP during all PSC seasons since 2012.

4. Conclusions

Understanding the spatial and temporal distribution of polar stratospheric clouds is important for the characterization of stratospheric ozone depletion during polar spring. We have updated our OMPS LP PSC detection algorithm to more reliably identify PSCs during winter and spring in

each hemisphere. Use of concurrent MLS H_2O and HNO_3 data to establish the NAT existence temperature threshold for each LP sample provides a more accurate representation of localized variations in PSC occurrence. We find that PSC areal coverage is consistent in both duration and magnitude in the Southern Hemisphere, but quite variable in the Northern Hemisphere, in agreement with previous observations (e.g. Pitts et al., 2018). We compare our OMPS LP PSC product with CALIOP PSC data for validation. While the full CALIOP PSC product has greater spatial coverage because lidar measurements can be made during polar night, the OMPS LP results are comparable to CALIOP PSC geographic distribution and seasonal coverage when the latitude range is limited to LP daytime sampling. Selected coincidence comparisons show that the assumed vertical extent of LP PSCs is generally consistent with the presence of liquid NAT particles identified by CALIOP. Our analysis also shows that the highest levels of PSC abundance (as measured by integrated PSC volume) occurred in 2023 when Hunga Tonga water vapor was likely present in the vortex before dehydration began (Millán et al., 2024).

The NH PSC variability is directly related to the high level of planetary wave activity in the Northern Hemisphere. OMPS LP also observes high clouds in locations where nominal FP-IT temperatures are too warm for PSC existence. These anomalies are often co-located with mountain topography, suggesting that the PSCs are triggered by mountain waves (Orr et al., 2020; Weimer et al., 2021). The significant increase in PSC identification observed with a 3 K adjustment to the FP-IT temperature suggests an approximate value for orographic gravity wave temperature perturbations in the lower stratosphere. This value is consistent with balloon and satellite gravity wave temperature observations (Schoeberl et al., 2017; Alexander et al., 2008; Alexander and Barnet, 2006).

The OMPS LP data record will continue with a second instrument now flying on the NOAA-21 satellite, as well as additional LP instruments on JPSS-4 (scheduled launch 2027) and JPSS-3 (scheduled launch 2032). While the OMPS LP limb scattering measurements have latitude sampling limitations similar to previous occultation instruments, their spatial sampling is more comprehensive. Since the CALIPSO mission has now ended, the OMPS LP PSC product represents an important extension of this record. These instruments will be operating after the end of the Aura MLS mission, so concurrent H_2O and HNO_3 profiles will not be available to calculate T_{NAT} and we will have to use reference profiles for our PSC detection algorithm. One option that we will investigate is the use of potential vorticity data to map H_2O climatology values into equivalent latitude to follow the polar vortex (e.g. Lait et al., 1990). We anticipate that using the LP instruments, we can extend our PSC data sets into the future.

Acknowledgements

This work was supported by NASA grant 80NSSC21K1965.

Open Research Section

S-NPP OMPS LP V2.1 aerosol data is available at (Taha, 2022).
MLS V5 H2O data are available at (Lambert et al., 2020).
MLS V5 HNO3 data are available at (Manney et al., 2020).
MLS V5 O3 data are available at (Schwartz et al., 2020).

CALIOP V2 PSC data are available at (NASA/LARC/SD/ASDC, 2024).
OMPS LP PSC software are available at (DeLand, 2025a).
S-NPP OMPS LP PSC daily data files are available at (DeLand, 2025b).

References

Alexander, M. J., and Barnet, C. (2006). Using satellite observations to constrain parameterizations of gravity wave effect for global models. *Journal of the Atmospheric Sciences*, *64*(5), 1-30, https://doi.org/10.1175/JAS3897.1

Alexander, M. J., Gille, J., Cavanaugh, C., Coffey, M., Craig, C., Eden, T., et al. (2008). Global estimates of gravity wave momentum flux from High Resolution Dynamics Limb Sounder observations. *Journal of Geophysical Research*, *113*, D15S18, https://doi.org/10.1029/2007JD008807

Carslaw, K. S., Luo, B. P., Clegg, S. L., Peter, Th., Brimblecombe, P., & Crutzen, P. J. (1994). Stratospheric aerosol growth and HNO_3 gas phase depletion from coupled HNO_3 and water uptake by liquid particle. *Geophysical Research Letters*, *21*, 2479-2482.

Chen, Z., DeLand, M., & Bhartia, P. K. (2016). A new algorithm for detecting cloud height using OMPS/LP measurements. *Atmospheric Measurement Techniques*, *9*, 1239-1246, https://doi.org/10.5194/amt-9-1239-2016

DeLand, M. (2025a). OMPS LP PSC Code [Software], Accessed: 15 January 2025. Zenodo, https://doi.org/10.5281/zenodo.14658867

DeLand, M. (2025b). S-NPP OMPS LP PSC Data [Data set], Accessed: 16 January 2025. Zenodo, https://doi.org/10.5281/zenodo.14673680

DeLand, M. T., Bhartia, P. K., Kramarova, N., & Chen, Z. (2020). OMPS LP observations of PSC variability during the NH 2019-2020 season. *Geophysical Research Letters*, *47*, e2020GL090216, https://doi.org/10.1029/2020GL090216

Gelaro, R., McCarty, W., Suárez, M. J., Todling, R., Molod, A., Takacs, L., et al. (2017). The Modern-Era Retrospective Analysis for Research and Applications, version 2 (MERRA-2). *Journal of Climate*, *30*, 5419-5454, https://doi.org/10.1175/JCLI-D-16-0758.1

Hanson, D. R., & Mauersberger, K. (1988). Laboratory studies of the nitric acid trihydrate: Implications for the south polar stratosphere. *Geophysical Research Letters*, *15*, 855-858, https://doi.org/10.1029/GL015i008p00855

Jaross, G., Bhartia, P. K., Chen, G., Kowitt, M., Haken, M., Chen, Z., et al. (2014). OMPS Limb Profiler instrument performance assessment. *Journal of Geophysical Research Atmospheres*, *119*, 4399-4412, https://doi.org/10.1002/2013JD020482

Kramarova, N. A., Bhartia, P. K., Jaross, G., Moy, L., Xu, P., Chen, Z., et al. (2018). Validation of ozone profile retrievals derived from the OMPS LP version 2.5 algorithm against correlative satellite measurements. *Atmospheric Measurement Techniques*, *11*, 2837-2861, https://doi.org/10.5194/amt-11-2837-2018

Lait, L. R., Schoeberl, M. R., Newman, P. A., Proffitt, M. H., Loewenstein, M., Podolske, J. R., et al. (1990). Reconstruction of O_3 and N_2O fields from ER-2, DC-8, and balloon

observations. *Geophysical Research Letters*, *17*, 521-524, https://doi.org/10.1029/GL017i004p00521

Lambert, A., Read, W., & Livesey, N. (2020). MLS/Aura Level 2 Water Vapor (H2O) Mixing Ratio V005, Greenbelt, MD, USA, Goddard Earth Sciences Data and Information Services Center (GES DISC), [Data set]. Accessed: 15 December 2024, https://doi.org/10.5067/Aura/MLS/DATA2508

Lambert, A., Read, W. G., Livesey, N. J., Santee, M. L., Manney, G. L., Froidevaux, L., et al. (2007). Validation of the Aura Microwave Limb Sounder middle atmosphere water vapor and nitrous oxide measurements. *Journal of Geophysical Research*, *112*, D24S36, https://doi.org/10.1029/2007JD008724

Livesey, N. L., Read, W. G., Wagner, P. A., Froidevaux, L., Santee, M. L., Schwartz, M. J., et al. (2022). *Earth Observing System (EOS) Aura Microwave Limb Sounder (MLS) Version 5.0x Level 2 and 3 data quality and description document*. JPL D-105336 Rev. B, Jet Propulsion Laboratory, Pasadena, CA.

Loughman, R., Bhartia, P. K., Chen, Z., Xu, P., Nyaku, E., & Taha, G. (2018). The Ozone Mapping and Profiler Suite (OMPS) Limb Profiler (LP) Version 1 aerosol extinction retrieval algorithm: theoretical basis. *Atmospheric Measurement Techniques*, *11*, 2633-2651, https://doi.org/10.5194/amt-11-2633-2018

Manney, G., Santee, M., Froidevaux, L., Livesey, N., & Read, W. (2020). MLS/Aura Level 2 Nitric Acid (HNO3) Mixing Ratio V005, Greenbelt, MD, USA, Goddard Earth Sciences Data and Information Services Center (GES DISC), [Data set]. Accessed: 15 December 2024, https://doi.org/10.5067/Aura/MLS/DATA2511

Manney, G. L., Livesey, N. J., Santee, M. L., Froidevaux, L., Lambert, A., Lawrence, Z. D., et al. (2020). Record-low Arctic stratospheric ozone in 2020: MLS observations of chemical processes and comparisons with previous extreme winters. *Geophysical Research Letters*, *47*, e2020GL089063, https://doi.org/10.1029/2020GL089063

Millán, L., Read, W. G., Santee, M. L., Lambert, A., Manney, G. L., Neu, J. L., et al. (2024) The evolution of the Hunga hydration in a moistening stratosphere. *Earth and Space Science Open Archive,* https://doi.org/10.22541/essoar.171201070.05823623/v1

Molleker, S., Borrmann, S., Schlager, H., Luo, B., Frey, W., Klingebiel, M., et al. (2014). Microphysical properties of synoptic-scale polar stratospheric clouds: in situ measurements of unexpectedly large HNO_3-containing particles in the Arctic vortex. *Atmospheric Chemistry and Physics*, *14*, 10785-10801, https://doi.org/10.5194/acp-14-10785-2014

NASA/LARC/SD/ASDC (2024). CALIPSO Lidar level 2 Polar Stratospheric Clouds presence, composition, and optical properties, V2-00 [Data set]. NASA Langley Atmospheric Science Data Center DAAC, Accessed: 10 June 2024. https://doi.org/10.5067/CALIOP/CALIPSO/CAL_LID_L2_PSCMASK-STANDARD-V2-00

Orr, A., Hosking, J. S., Delon, A., Hoffmann, L., Spang, R., Moffat-Griffin, T., et al. (2020) Polar stratospheric clouds initiated by mountain waves in a global chemistry–climate model: a

missing piece in fully modelling polar stratospheric ozone depletion, *Atmospheric Chemistry and Physics*, *20*, 12483–12497, https://doi.org/10.5194/acp-20-12483-2020.

Pitts, M. C., Poole, L. R., & Gonzalez, R. (2018). Polar stratospheric cloud climatology based on CALIPSO spaceborne lidar measurements from 2006 to 2017. *Atmospheric Chemistry and Physics*, *18*, 10881-10913, https://doi.org/10.5194/acp-18-10881-2018

Poole, L. R., Trepte, C. R., Harvey, V. L., Toon, G. C., & VanValkenburg, R. L. (2003). SAGE III observations of Arctic polar stratospheric clouds – December 2002. *Geophysical Research Letters*, *30*, 2216, https://doi.org/10.1029/2003GL018496

Rex, M., Salawitch, R. J., Deckelmann, H., van der Gathen, P., Harris, N. R. P., Chipperfield, M. P., et al. (2006). Arctic winter 2005: Implications for stratospheric ozone loss and climate change. *Geophysical Research Letters*, *33*, L23808, https://doi.org/10.1029/2006GL026731

Santee, M. L., Lambert, A., Read, W. G., Livesey, N. J., Cofield, R. E., Cuddy, D. T., et al. (2007). Validation of the Aura Microwave Limb Sounder HNO_3 measurements. *Journal of Geophysical Research*, *112*, D24S40, https://doi.org/10.1029/2007JD008721

Schoeberl, M. R., Jensen, E., Podglajen, A., Coy, L., Lodha, C., Candido, S., & Carver, R. (2017). Gravity wave spectra in the lower stratosphere diagnosed from project loon balloon trajectories. *Journal of Geophysical Research – Atmospheres*, *122*, 8517-8524, https://doi.org/10.1002/2017JD026471

Schoeberl, M., Jensen, E., Wang, T., Taha, G., Ueyama, R., Wang, Y., et al. (2021). Cloud and aerosol distributions from SAGE III/ISS observations. *Journal of Geophysical Research: Atmospheres*, *126*, e2021JD035550. https://doi.org/10.1029/2021JD035550

Schwartz, M., Froidevaux, L., Livesey, N., & Read, W. (2020). MLS/Aura Level 2 Ozone (O3) Mixing Ratio V005, Greenbelt, MD, USA, Goddard Earth Sciences Data and Information Services Center (GES DISC), [Data set]. Accessed: 15 December 2024, https://doi.org/10.5067/Aura/MLS/DATA2516

Solomon, S. (1999). Stratospheric ozone depletion: A review of concepts and history. *Reviews of Geophysics*, *37*, 275-316, https://doi.org/10.1029/1999RG900008

Strahan, S. E., Douglass, A. R., & Steenrod, S. D. (2016). Chemical and dynamical impacts of stratospheric sudden warmings on Arctic ozone variability. *Journal of Geophysical Research Atmospheres*, *121*, 11,836-11,851, https://doi.org/10.1002/2016JD025128

Taha, G. (2022). OMPS-NPP LP L2 Aerosol Extinction Vertical Profile swath multi-wavelength daily 3slit Collection V2.0 Version 2.1, Greenbelt, MD, USA, Goddard Earth Sciences Data and Information Center (GES DISC), [Data set]. Accessed: 15 December 2024. https://doi.org/10.5067/CX2B9NW6FI27

Taha, G., Loughman, R., Zhu, T., Thomason, L., & Jaross, G. (2022). Tracking the 2022 Hunga Tonga-Hunga Ha'apai aerosol cloud in the upper and middle stratosphere using space-based observations. *Geophysical Research Letters*, *49*, e2002GL100091, https://doi.org/10.1029/2022GL100091

Taha, G., Loughman, R., Zhu, T., Thomason, L., Kar, J., Rieger, L., & Bourassa, A. (2021). OMPS LP Version 2.0 multi-wavelength aerosol extinction coefficient retrieval algorithm.

Atmospheric Measurement Techniques, *14*, 1015-1036, https://doi.org/10.5194/amt-14-1015/2021

Thomason, L. W., & Vernier, J.-P. (2013). Improved SAGE II cloud/aerosol categorization and observations of the Asian tropopause aerosol layer:1989–2005, *Atmospheric Chemistry and Physics*, *13*, 4605–4616, https://doi.org/10.5194/acp-13-4605-2013

Tritscher, I., Pitts, M. C., Poole, L. R., Alexander, S. P., Cairo, F., Chipperfield, M. P., et al. (2021). Polar stratospheric clouds: Satellite observations, processes, and role in ozone depletion. *Reviews of Geophysics*, *59*, e2020RG000702, https://doi.org/10.1029/2020RG000720

Waibel, A. E., Peter, Th., Carslaw, K. S., Oelhaf, K., Wetzel, G., Crutzen, P. J., et al. (1999). Arctic ozone loss due to denitrification. *Science*, *283*, 2064-2069, https://doi.org/10.1126/science.283.5410.2064

Weimer, M., Buchmüller, J., Hoffmann, L., Kirner, O., Luo, B., Ruhnke, R., et al. (2021). Mountain-wave-induced polar stratospheric clouds and their representation in the global chemistry model ICON-ART. *Atmospheric Chemistry and Physics*, *21*, 9515–9543, https://doi.org/10.5194/acp-21-9515-2021

Waugh, D. W., Sobel, A. H., & Polvani, L. M. (2017). What is the polar vortex and how does it influence weather. *Bulletin American Meteorological Society*, *98*, 37-44, https://doi.org/10.1175/BAMS-D-15-00212.1

Winker, D. M., Vaughan, M. A., Omar, A. H., Hu, Y., Powell, K. A., Liu, Z., et al. (2009). Overview of the CALIPSO mission and CALIOP data processing algorithms. *Journal of Atmospheric and Oceanic Technology*, *26*, 2310-2323, https://doi.org/10.1175/2009JTECHA1281.1

World Meteorological Organization (WMO) (2022). *Scientific Assessment of Ozone Depletion: 2022*. GAW Report No. 278, 509 pp. WMO: Geneva.